

A novel, optimized approach of voxel division for water vapor tomography

Yibin Yao^{1,2,3} · Qingzhi Zhao¹

Received: 18 September 2015 / Accepted: 15 March 2016 / Published online: 26 March 2016
© Springer-Verlag Wien 2016

Abstract Water vapor information with highly spatial and temporal resolution can be acquired using Global Navigation Satellite System (GNSS) water vapor tomography technique. Usually, the targeted tomographic area is discretized into a number of voxels and the water vapor distribution can be reconstructed using a large number of GNSS signals which penetrate the entire tomographic area. Due to the influence of geographic distribution of receivers and geometric location of satellite constellation, many voxels located at the bottom and the side of research area are not crossed by signals, which would undermine the quality of tomographic result. To alleviate this problem, a novel, optimized approach of voxel division is here proposed which increases the number of voxels crossed by signals. On the vertical axis, a 3D water vapor profile is utilized, which is derived from radiosonde data for many years, to identify the maximum height of tomography space. On the horizontal axis, the total number of voxel crossed by signal is enhanced, based on the concept of non-uniform symmetrical division of horizontal voxels. In this study, tomographic experiments are implemented using GPS data from Hong Kong Satellite Positioning Reference Station Network, and tomographic result is compared with

water vapor derived from radiosonde and European Center for Medium-Range Weather Forecasting (ECMWF). The result shows that the Integrated Water Vapour (IWV), RMS, and error distribution of the proposed approach are better than that of traditional method.

1 Introduction

Water vapor covers a very small portion of the total atmospheric volume, but plays a very important role in maintaining atmospheric vertical distribution, as well as the formation of clouds and rain (Wang et al. 2014; Yao et al. 2016). Knowing water vapor information with highly temporal and spatial resolution is a prerequisite for prevention of the medium-to-small-scaled weather disastrous. In the past, the main tools for acquiring water vapor are radiosonde, microwave radiometer, and so on. However those methods are confined by their disadvantages, such as low temporal and spatial resolution, as well as high construction and maintenance costs. Consequently, water vapor information obtained by traditional methods is limited in terms of temporal and spatial resolution (Wan 2014).

The arrival of the GNSS tomographic technique provides a new method to acquire water vapor information with highly temporal and spatial resolution (Bevis et al. 1992). Since the validity of water vapor information obtained from GPS-observed data was confirmed by Bevis et al. (1992), the development of water vapor tomography technique has advanced by leaps and bounds (Flores et al. 2000; Troller et al. 2002; Champollion et al. 2009; Perler et al. 2011; Chen and Liu 2014; Adavi and Mashhadi-Hossainali 2014; Rohm et al. 2014). Due to the specific distribution of satellite constellation and receivers, as well

Responsible Editor: R. Roebeling.

✉ Yibin Yao
ybyao@whu.edu.cn

- ¹ School of Geodesy and Geomatics, Wuhan University, Wuhan 430079, China
- ² Key Laboratory of Geospace Environment and Geodesy, Ministry of Education, Wuhan University, Wuhan 430079, China
- ³ Collaborative Innovation Center for Geospatial Technology, Wuhan 430079, China

as the specific choice of tomography area, the number of signals that passing through the whole tomographic area is limited. Ultimately, many voxels are not crossed by signal rays, especially those locate at periphery and lower space of the tomographic area. Chen and Liu (2014) proposed a method to improve the utilization of signal rays by moving the tomographic area according to the specific tomography condition. However, this approach is limited by the need to relocate the tomographic area before every tomography experiment according to the number of signals crossed the test area, which is hard to operate in practice.

To ensure maximal use of signal rays crossing the entire tomographic area, a novel approach with the advantage of easy operation is proposed. In our study, the maximum tomographic height is determined by radiosonde data over 40 years. In horizontal direction, the horizontal resolution for the target area is selected on the basis of non-uniform symmetrical division of horizontal voxels. Finally, the proposed approach was validated using data from Hong Kong Satellite Positioning Reference Station Network.

2 The principle of tomography

2.1 Building of observation equation

There are two classes of observations derived from GNSS-based receivers can be used for tropospheric tomography; first is slant wet delay (SWD), which can be used to acquire wet refractivity values (Flores et al. 2000; Skone and Hoyle 2005; Rohm and Bosy 2009; Notarpietro et al. 2011), and second is slant water vapor (SWV), which can be exploited to obtain the water vapor distribution information (Champollion et al. 2005; Chen and Liu 2014). Tomographic results derived from two classes of observation can be crossed-converted, based on the atmospheric temperature field (Bender et al. 2011). For our study, SWV is used to obtain three-dimensional water vapor information.

SWD is determined by wet refractivity value along a given slant path, and often refers to the wet delay on a given satellite signal time lapse from satellite to GNSS-based receiver, and can be expressed as follows (Flores et al. 2000):

$$SWV = 10^{-6} \times \int_s \rho_w ds \quad (1)$$

where s is the propagation path of satellite signal. N_{wet} is the atmospheric wet refractivity (unit: mm/km). SWD can be obtained by processing the observation derived from GNSS-based receivers.

In our study, GAMIT (v10.50) (Herring et al. 2010) software was used for processing the GPS observation based on double-differenced model, and Niell mapping function was adopted. The interval of Zenith Tropospheric

Delay (ZTD) and gradient parameters estimated was 30 min, and the elevation cut-off angle of 10° was selected so as to ignore the influence of ray bending on tomographic result (Mendes 1999). Due to the short baseline between receivers in the local region, the similar propagated paths of signals received by different stations and a strong correlation of the signal delay above the atmosphere among stations are existed. To reduce the correlation of tropospheric parameters among the network, three stations are introduced (BJFS, LHAZ and SHAO) with the length of baseline larger than 500 km (Rocken et al. 1995). By combining the surface pressure, the accurate Zenith Hydrostatic Delay (ZHD) can be calculated based on the empirical model (Saastamoinen 1972):

$$ZHD = \frac{0.002277 \times P_s}{1 - 0.00266 \times \cos(2\varphi) - 0.00028 \times H} \quad (2)$$

where P_s is surface pressure (unit: hPa), φ is the latitude of station, H is the geodetic height. Therefore, the Zenith Wet Delay (ZWD) would be separate from the ZTD by minus the ZHD, and the Slant Wet Delay (SWD) can be obtained as follows (Flores et al. 2000):

$$SWD_{ele,\varphi} = m_{wet}(elv) \times ZWD + m_{wet}(elv) \times \cot(elv) \times (G_{NS}^w \times \cos \varphi + G_{WE}^w \times \sin \varphi) + R_e \quad (3)$$

where elv is satellite elevation, φ is azimuth, m_{wet} is the wet mapping function, G_{WE}^w and G_{NS}^w are wet delay gradient parameters in the east–west and north–south directions, R_e is the unmodelled residuals, which is obtained according to the method proposed by Alber et al. (2000).

Therefore, SWD can be converted to SWV by following formula (Chen and Liu 2014):

$$SWV = \frac{10^6}{\rho_{water} R_w [(k_3/T_m) + k_2']} \times SWD \quad (4)$$

where $k_2' = 16.48K \text{ hPa}^{-1}$, $k_3 = 3.776 \times 10^5 K^2 \text{ hPa}^{-1}$, $R_w = 461 (\text{J kg}^{-1} \text{ K}^{-1})$ and are the specific gas constants for water vapor. ρ_{water} is water vapor density (unit: g/m^3). T_m is the weighted mean tropospheric temperature, in our study, T_m is the empirical formula, which is calculated by Liu et al. (2001) using the meteorological measurements.

Once SWV is obtained, the tomographic area can be discretized into a number of voxels, in which water vapor density is a constant in voxels over a given period of time. Therefore, SWV of signal propagation path can be discretized as follows (Chen and Liu 2014):

$$SWV^p = \sum_{ijk} (d_{ijk}^p \cdot \rho_{ijk}) \quad (5)$$

where SWV^p is the slant water vapor of p th signal path (unit: mm). i, j, k are the position of tomographic voxel in

longitude, latitude and vertical directions. d_{ijk}^p is the distance of p th signal in voxel (i, j, k) (unit: km). ρ_{ijk} is the water vapor density in a given voxel (i, j, k) (unit: g/m^3). The above equation can be written in matrix form as follows (Flores et al. 2000; Chen and Liu 2014):

$$y_{m \times 1} = A_{m \times n} \cdot \rho_{n \times 1} \tag{6}$$

where m is the number of total SWVs, while n is the number of voxels in the tomographic area. y is the observation, refers to SWV here which penetrate the whole research area, while A is the coefficient matrix of signal transit distances through the voxels and ρ is the column vector of unknown, which refers to water vapor density in our study.

2.2 Constraint equation

To acquire the water vapor density value in Eq. (6), an inversion algorithm needs to be performed. However, many voxels in the tomographic area are not crossed by any signals. Matrix A in Eq. (6) is very a large sparse matrix, and water vapor information for those voxels that rays do not pass through are lost. To overcome this rank deficiency problem, the mostly widely-used method is to impose constraint information (Bi et al. 2006). In our study, the horizontal constraint equation is imposed based the Gauss-weighted functional method (Song et al. 2006) while the functional relationship of exponential distribution is established among the voxels on the vertical direction (Elósegui et al. 1998).

The horizontal constraint equation is as follows (Song et al. 2006):

$$H_1\rho_1 + H_2\rho_2 + \dots + H_{j-1}\rho_{j-1} - \rho_j + H_{j+1}\rho_{j+1} = 0 \tag{7}$$

where, ρ is the water vapor density, H is the coefficient of horizontal constraint equation which is computed by the following formula:

$$H_{i,j,k}^{i_1,j_1,k_1} = \begin{cases} 1, (i = i_1 \& j = j_1) \\ - \frac{\exp\left(-\frac{d_{i_1,j_1,k_1}^2}{2\sigma^2}\right)}{\sum_i \sum_j \exp\left(-\frac{d_{i_1,j_1,k_1}^2}{2\sigma^2}\right)}, (i \neq i_1 / j \neq j_1) \\ 0, (k \neq k_1) \end{cases} \tag{8}$$

As mentioned above, i, j, k are the positions of operational voxel while i_1, j_1, k_1 are the marks of other voxels in three directions. d_{i_1,j_1,k_1} is the distance between the operated voxel and some other voxels. σ is smooth factor. Therefore, the matrices form of horizontal constraint can be written as follows:

$$H_{m \times n} \cdot \rho_{n \times 1} = \mathbf{0}_{m \times n} \tag{9}$$

where H is the coefficient matrix of horizontal constraint.

The vertical constraint equation is established based on the following relation (Elósegui et al. 1998):

$$\rho_i / \rho_{i-1} = e^{(h_{i-1}-h_i)/H} \tag{10}$$

where ρ_i and h_i is the water vapor density and the height of the i th layer, separately. H is the water vapor scale height, which is selected to be 1–2 km. Therefore, the coefficient between two adjacent voxels vertically can be obtained as follows:

$$v_i = e^{(h_{i-1}-h_i)/H} - 1 \tag{11}$$

where v_i is the coefficient of vertical constraint between the i th and $(i - 1)$ th layer. The matrices form of vertical constraint can be written as follows:

$$V_{m \times n} \cdot \rho_{n \times 1} = \mathbf{0}_{m \times n} \tag{12}$$

where V is the coefficient matrix of horizontal constraint.

Consequently, the final tomographic model can be acquired by combining formulas (6), (9) and (12) as follows:

$$\begin{pmatrix} A_{m \times n} \\ H_{m \times n} \\ V_{m \times n} \end{pmatrix} \cdot \rho_{n \times 1} = \begin{pmatrix} y_{m \times n} \\ \mathbf{0}_{m \times n} \\ \mathbf{0}_{m \times n} \end{pmatrix} \tag{13}$$

Following the singular value decomposition method, the general inverse matrix can be obtained (Ran and Ge 1997).

3 Tomographic voxel optimization

Atmospheric water vapor at a given altitude varies over changing geographic tomography area. In addition, the quality of tomographic result is affected by the division of the tomographic voxels, and unreasonable division of tomographic voxels would lead to the tomographic result divergent from actual water vapor distribution (Bi et al. 2006; Notarpietro et al. 2011). Consequently, the vertical height for a tomographic area should be determined according to the actual conditions of the research area, and the voxels also should be reasonably discretized.

3.1 Determination of vertical boundary

The most part of atmospheric water vapor is concentrated in the troposphere (Mohanakumar 2008), and the distribution of which cannot be expressed by a uniform formula. Decreasing with height, however, water vapor tend to zero gradually. For most tomographic experiments in the past, the vertical boundary was selected based upon the researcher’s experience. Yet, over various research areas, the distribution of water vapor varies differently. For

example, water vapor value is close to zero at 8 km altitude in some areas, while water vapor concentration is still very high at the height of 10 km in other areas. In accord with change in actual water vapor distribution on the vertical direction of the test area, maximum vertical height should therefore be determined which is essential to the effective use tomographic observation.

Assuming a case that the vertical resolution is 0.8 km, using 8 km as the vertical boundary (10 voxels vertically) of tomographic area can save 23.1 % of unknowns than that of selecting vertical boundary 10.4 km (13 voxels vertically). The lower the vertical boundary of tomographic area selected is, the greater the number of signals crossing the whole area that can be used. As shown in Fig. 1, signals which pass through the gray area can also be utilized when the vertical boundary drops from 10.4 to 8 km. However, if the vertical boundary of tomographic area is too low, the influence of water vapor above vertical boundary to tomographic result is ignored, which causes the tomographic result deviate from actual conditions.

To make a direct comparison of signal utilization and the number of voxels crossed by signals for various selected vertical boundaries, two schemes were designed for this experiment as follows

Scheme 1, vertical height is 10.4 km, vertical resolution is 0.8 km, total voxels is $8 \times 7 \times 13$;

Scheme 2, vertical height is 8 km, vertical resolution is 0.8 km, total voxels is $8 \times 7 \times 10$.

First we analyzed the observed data from GPS network from Hong Kong at Day of Year (DOY) 139. Figure 2 gives the number of signals used once per hour. Figure 3 gives the percentage of voxels crossed by signals. The calculation shows that the average utilization of signals increased by 7.51 %, from 51.51 % (Scheme 1) to 59.02 % (Scheme 2), once the vertical boundary was lowered from 10.4 to 8 km. In addition, the percentage of voxels crossed by signals also increased by 2.73 %. Subsequently, we analyzed the data for 31 days of DOY 121 to 151, 2013. Figure 4 gives the number of signals used once per day, while Fig. 5 gives the percentage of voxels crossed by

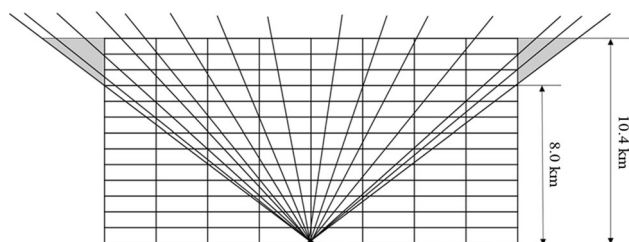


Fig. 1 Schematic plan of signals rays passing through tomographic area

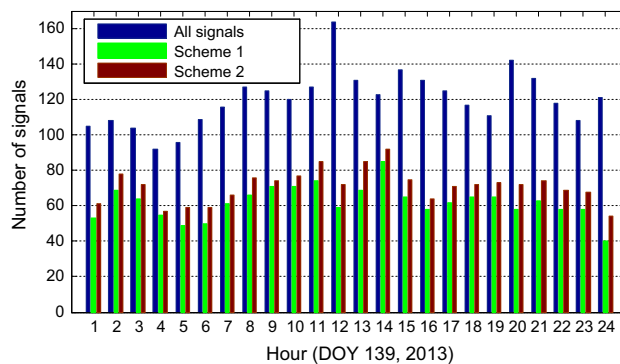


Fig. 2 Number of signals used for scheme A and B once per hour at DOY 139, 2013

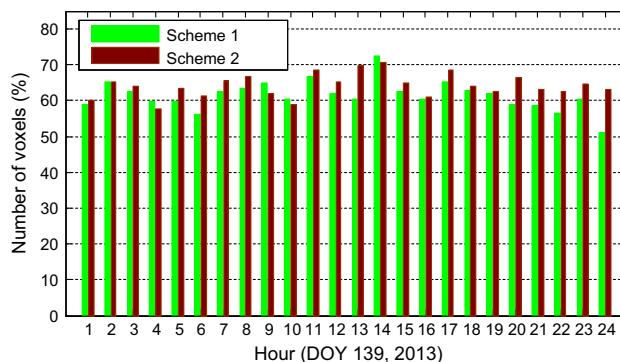


Fig. 3 Number of voxels crossed by signal rays for scheme A and B once per hour at DOY 139, 2013

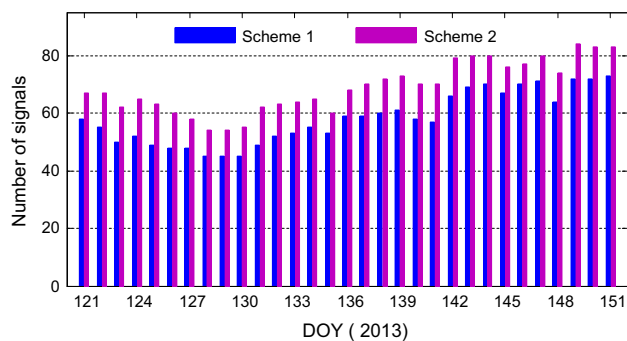


Fig. 4 Average number of signals used for scheme A and B for 31 days of DOY 121 to 151, 2013

signals. Here, calculation shows that the average utilization of signals increased by 8.69 % from 47.44 % (Scheme 1) to 56.13 % (Scheme 2), once the vertical boundary was lowered from 10.4 to 8 km. In addition, the percentage of voxels crossed by signals also increased by 6.52 %. Consequently, in terms of utilization of signal rays, reasonable choice of vertical boundary plays an important role in using as much of existing observation as possible and improving the number of voxels crossed by signals.

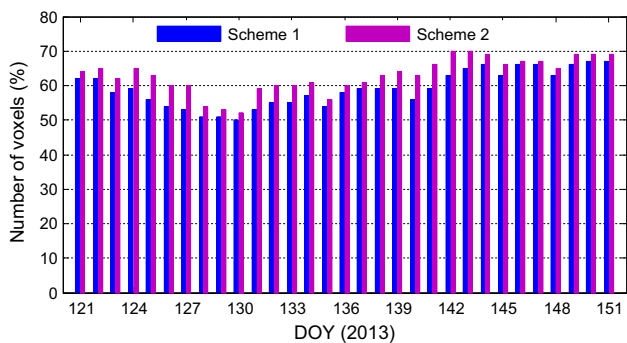


Fig. 5 Average number of voxels crossed by signal rays for scheme A and B for 31 days of DOY 121 to 151, 2013

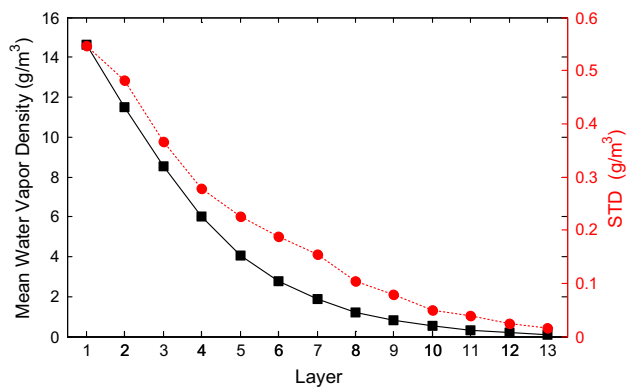


Fig. 6 Average water vapor density and STD from radiosonde 45004 for 40 years from 1974 to 2014

Radiosonde data can provide accurate water vapor profiles at different altitudes (Niell et al. 2001; Adeyemi and Joerg 2012). In our study, therefore, the vertical boundary is determined on the basis of 3D water vapor distribution derived from radiosonde for many years. There is a radiosonde station 45004 in King’s Park of Hong Kong, from which average vertical water vapor profile and STD for 40 years (1974–2014) are given in Fig. 6. It can be seen in Fig. 6 that water vapor density is less than 0.2 g/m³ over the height of 8 km (10th layer), while the STD is less than 0.05 g/m³. Consequently, 8 km was selected as the vertical boundary of tomographic area for our study.

3.2 Non-uniform symmetrical division of horizontal voxel

For the purpose of convenience, past tomography studies divided voxels on the horizontal direction by uniform horizontal spacing, which leads to a great differences in actual observed information among various voxels-relatively richer information in voxels centrally located in the tomographic area, and less to no observed information in lowest and peripheral voxels. Obtained as observed data

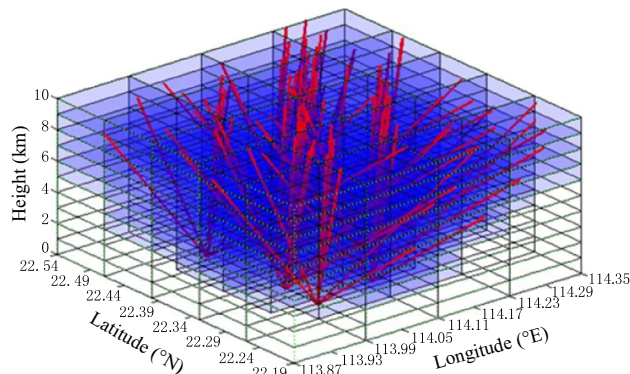


Fig. 7 Three dimensional distribution of signal rays crossing the tomographic area

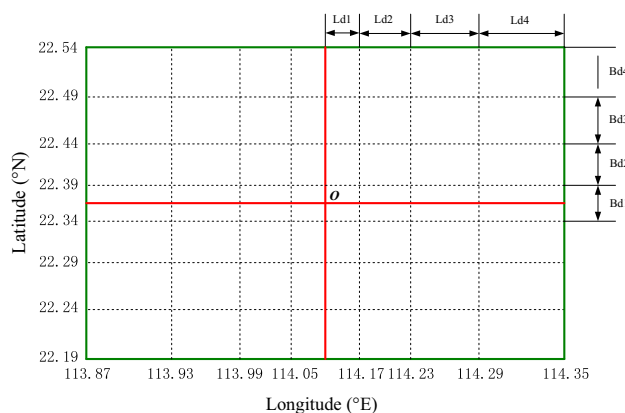


Fig. 8 Schematic representation of non-uniform symmetrical division of horizontal voxels

from 12 Hong Kong receiver stations at UTC 00:00 DOY 121, 2013, Fig. 7 gives the actual condition of signal distribution of tomographic area. Relative color depth covering the tomographic area corresponds positively to the frequency of signals crossed the voxels. It follows from Fig. 7 that more signals pass through the tomographic center, while fewer signals cross the edge and bottom of the tomographic area. In addition, many voxels positioned at the periphery and lowest altitudes of the tomographic area are not crossed by signals. To alleviate this phenomenon, a novel, approach of non-uniform symmetrical division of horizontal voxels is therefore proposed. Assuming that the center of the tomographic area as starting point, as shown by point O in Fig. 8, and combined the actual distribution of signal rays crossing the tomographic area, horizontal voxels are then dispersed by increment and symmetrical horizontal spacing along both longitudinal and latitudinal directions. Along both directions of longitude and latitude, the horizontal voxel spacing in Fig. 8 should adhere to the following relationship: $Ld1 \leq Ld2 \leq Ld3 \leq Ld4$, $Bd1 \leq Bd2 \leq Bd3 \leq Bd4$. Here,

Ld and Bd are the distance in latitude and longitude directions. Finally, the tomographic area is discretized into non-uniform symmetrical horizontal spaces. The central principle of this method is that for those more densely areas which signals passing through, a small horizontal spacing is exploited; while a relative wider spacing is used for those less densely areas that signals passing through, which makes the observed information evenly distributed among voxels as soon as possible.

Based on Sect. 3.1 and the idea of non-uniform symmetrical division of horizontal voxels, we consequently designed five schemes for tomographic experiment to validate the proposed method. scheme A is designed based on the idea of traditional uniform division of horizontal voxels. Schemes B–E are designed on the basis of non-uniform division of horizontal voxels following the principle that small horizontal spacing is exploited close to the center of tomographic area, while relative big horizontal spacing is utilized at the margin of tomographic area.

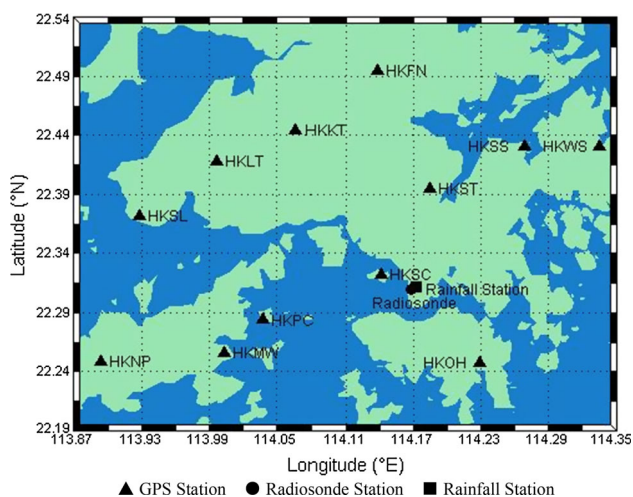


Fig. 9 The geographic distribution of Hong Kong GPS network, radiosonde station and rainfall station

Table 1 Specific information of Hong Kong satellite positioning reference station network

Station name	Latitude (°)	Longitude (°)	Height (m)	Receiver type
HKFN	22.2940	114.0817	41.134	LEICA GRX1200 + GNSS
HKKT	22.2641	114.0359	34.490	LEICA GRX1200 + GNSS
HKSS	22.2551	114.1609	38.634	LEICA GRX1200 + GNSS
HKOH	22.1451	114.1342	166.322	LEICA GRX1200 + GNSS
HKST	22.2342	114.1103	258.634	LEICA GRX1200 + GNSS
HKSC	22.1919	114.0828	20.152	LEICA GRX1200 + GNSS
HKPC	22.1705	114.0216	18.042	LEICA GRX1200 + GNSS
HKMW	22.1520	114.0011	194.871	LEICA GRX1200 + GNSS
HKLT	22.2505	113.5947	125.839	LEICA GRX1200 + GNSS
HKSL	22.2219	113.5540	95.212	LEICA GRX1200 + GNSS
HKWS	22.2603	114.2007	63.789	LEICA GRX1200 + GNSS
HKNP	22.1456	113.5337	350.611	LEICA GRX1200 + GNSS

The range of tomographic area in our study is latitude N22.19°–N22.54°, longitude E113.87°–E114.35°, while the vertical resolution is 0.8 km and the total number of voxels is $7 \times 8 \times 10$. The selected GPS stations are symbolized in Fig. 9 and their details are given in Table 1. The specific details of various schemes are shown in Table 2.

To analyze the influence of different approaches on the number of voxels crossed by signals, the experiments were performed. Figure 10 gives the statistical result for the number of voxels crossed by signals between schemes A and B, (a) shows the statistical result of once per day for the period of DOY 121 to 151, 2013, and (b) gives the result of once per hour at DOY 130, 2013. It can be seen from Fig. 10 that, under the condition that the number of signals crossed the tomographic area are same, the number of voxels was increased by exploiting the approach of non-uniform symmetrical division of horizontal voxels. Pertinent calculation shows that the average number of voxels increased by 9.06 % from 58.40 to 67.46 % under the method proposed here.

4 Validation of the proposed method

As mentioned above, an accurate water vapor profile can be acquired using radiosonde, which is often regarded as the reference of choice to evaluate water vapor information derived from other methods (Niell et al. 2001; Liu et al. 2013). As shown in Fig. 8, there is a radiosonde station 45004 in King's Park of study area, where the sounding balloon is launched every day at UTC 00:00 and 12:00. In addition, water vapor density value can also be obtained using data provided by ECMWF, which provides global reanalysis data four times per day at UTC 00:00, 06:00, 12:00 and 18:00. The resolution level of data provided by the ECMWF for our study is $0.125^\circ \times 0.125^\circ$, and there

Table 2 Specific information of steps in latitude and longitude directions for various schemes

Scheme	Latitude step (°)	Longitude step (°)
A	0.05, 0.05, 0.05, 0.05, 0.05, 0.05, 0.05	0.06, 0.06, 0.06, 0.06, 0.06, 0.06, 0.06, 0.06
B	0.07, 0.05, 0.04, 0.03, 0.04, 0.05, 0.07	0.08, 0.07, 0.05, 0.04, 0.04, 0.05, 0.07, 0.08
C	0.06, 0.06, 0.04, 0.03, 0.04, 0.06, 0.06	0.08, 0.07, 0.05, 0.04, 0.04, 0.05, 0.07, 0.08
D	0.07, 0.05, 0.04, 0.03, 0.04, 0.05, 0.07	0.07, 0.07, 0.06, 0.04, 0.04, 0.06, 0.07, 0.07
E	0.06, 0.06, 0.04, 0.03, 0.04, 0.06, 0.06	0.07, 0.07, 0.06, 0.04, 0.04, 0.06, 0.07, 0.07

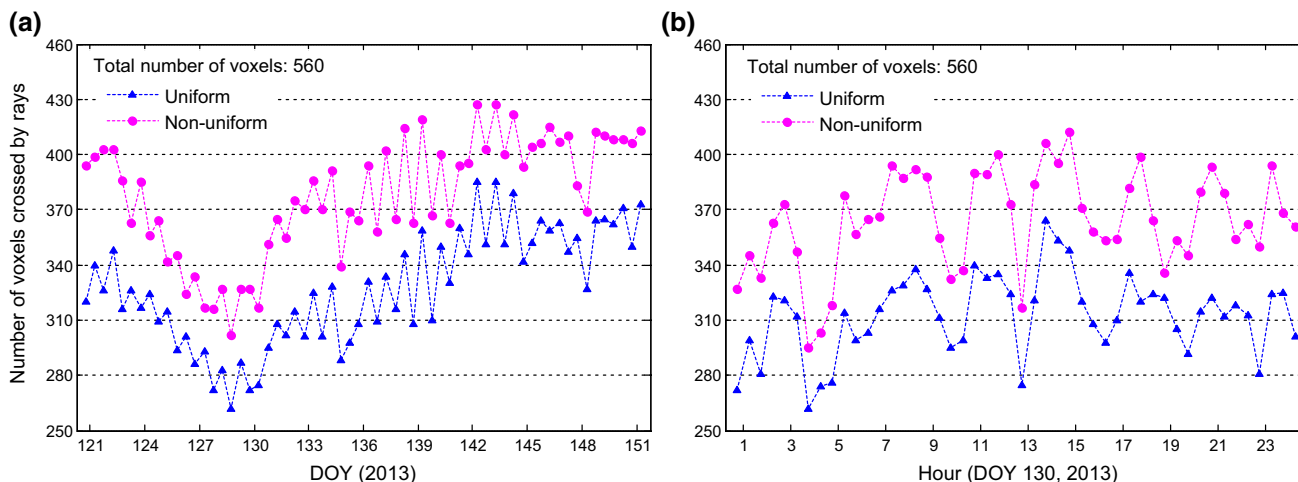


Fig. 10 Number of voxels crossed by rays under different division of horizontal voxel

Table 3 The geographic location of ECMWF grid point in Hong Kong

Grid point	Latitude (°)	Longitude (°)	Grid point	Latitude (°)	Longitude (°)
B1L1	22.250	113.875	B2L3	22.375	114.125
B1L2	22.250	114.000	B2L4	22.375	114.250
B1L3	22.250	114.125	B3L1	22.500	113.875
B1L4	22.250	114.250	B3L2	22.500	114.000
B2L1	22.375	113.875	B3L3	22.500	114.125
B2L2	22.375	114.000	B3L4	22.500	114.250

are twelve grid points in tomographic area. Table 3 gives the geographic location of grid points. Therefore, the result derived from radiosonde and ECMWF data are used to validate the tomographic result from different schemes with respect to the IWV, water vapor profile and error distribution.

4.1 IWV comparison

To make a direct comparison of integrated water vapor (IWV) derived from different schemes, the data covering 31 days for the period of DOY 121 to 151, 2013 is analyzed. To begin, IWV for the location of radiosonde station is calculated using the voxels information acquired from different tomographic schemes for the UTC 00:00 and

12:00 epoch, and then compared with IWV derived from radiosonde and ECMWF. Here, the Méso-NH model is used to compute the IWV by vertical integration of the water vapor content (ρ_w) through the model vertical layers (Brenot et al. 2006):

$$IWV = \int_L \rho_w dz \tag{14}$$

Figure 11 shows the IWV comparison between schemes A, B and radiosonde for the period of DOY 121 to 151, 2013. Figure 12 shows the IWV comparison between schemes A, B and ECMWF for the period of DOY 121 to 151, 2013. Tables 4 and 5 give the statistical result for five schemes compared with radiosonde and ECMWF during the same period. It can be seen from Figs. 11 and 12 that IWV derived from scheme B are in good agreement with

Fig. 11 Comparison of IWV time series derived from radiosonde and various tomographic result for the period of DOY 121 to 151, 2013

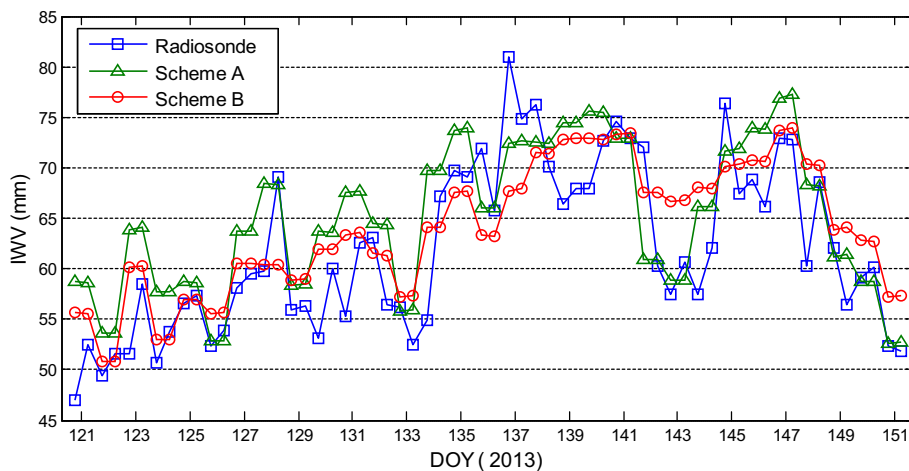


Fig. 12 Comparison of IWV time series derived from ECMWF and various tomographic result for the period of DOY 121 to 151, 2013

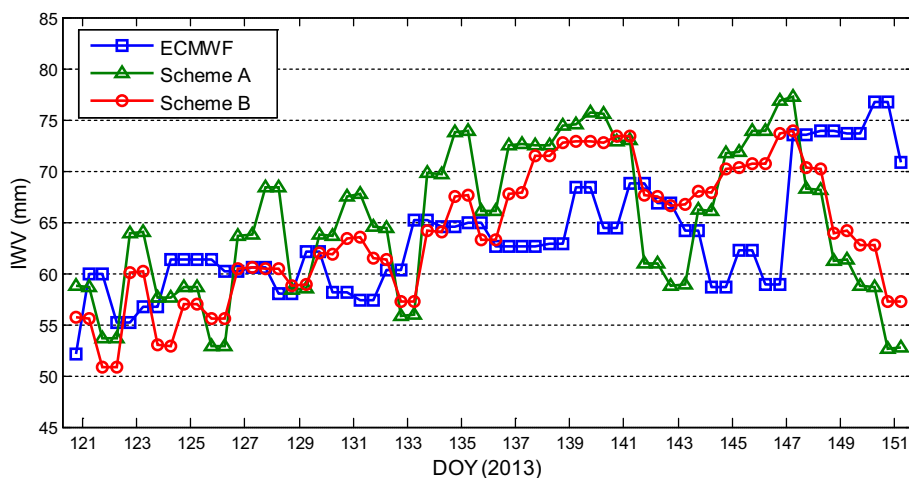


Table 4 Statistical result of IWV between various schemes and radiosonde for 31 days for the period of DOY 121 to 151, 2013

Scheme	A	B	C	D	E
RMS	5.71	5.12	5.19	5.06	5.07
STD	7.14	6.33	6.36	6.34	6.39
MAE	4.48	4.09	4.11	4.00	3.99
Bias	-3.04	-1.93	-1.89	-1.93	-1.86

Table 5 Statistical result of IWV between various schemes and ECMWF for 31 days for the period of DOY 121 to 151, 2013

Scheme	A	B	C	D	E
RMS	9.03	6.84	6.91	6.99	7.11
STD	7.14	6.33	6.36	6.34	6.39
MAE	7.70	5.40	5.46	5.56	5.69
Bias	-1.58	-0.48	-0.44	-0.47	-0.40

those from radiosonde and ECMWF, relative to those from scheme A. The statistical results from Tables 4 and 5 show that the RMS, STD, MAE and Bias of IWV calculated on the basis of non-uniform symmetrical division of horizontal voxels (scheme B–E) are superior to those of traditional method (scheme A).

4.2 Water vapor profile comparison

Although IWV results derived from schemes B–E agree well with those from the radiosonde, while also showing low RMS, STD, MAE and Bias, one may not conclude that the vertical water vapor distribution profile has been obtained correctly. For instance, if two vertical layers are exchanged arbitrarily, the calculated IWV value remains unchanged, but the vertical distribution of water vapor has changed. Therefore, to further test the accuracy of vertical water vapor density, water vapor profile comparisons between radiosonde, ECMWF and different schemes were

Fig. 13 Water vapor density profile derived from radiosonde, ECMWF and various tomographic result. Time period in **a** and **b** are 00:00 UTC DOY 121, 2013 and 12:00 UTC DOY 136, 2013, respectively

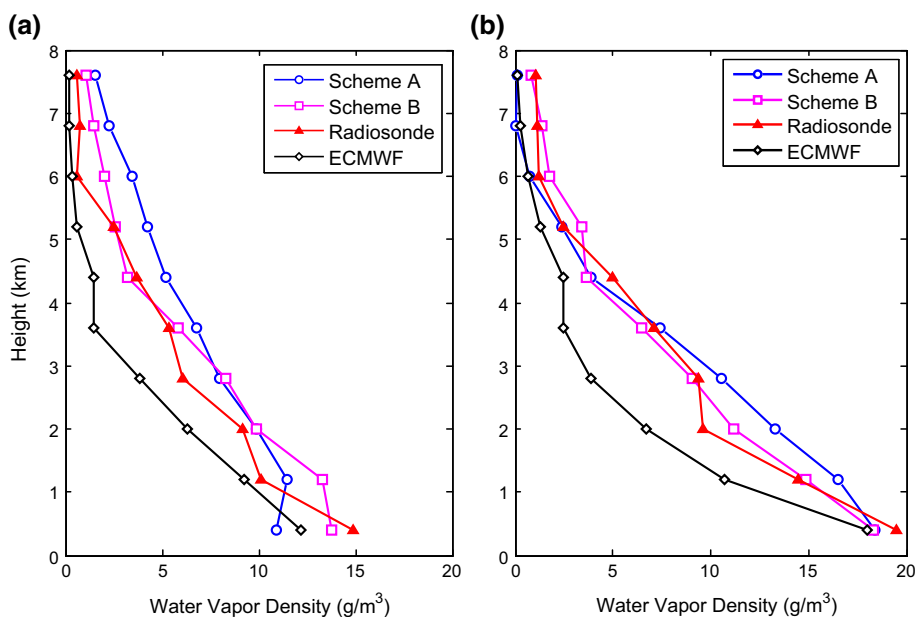
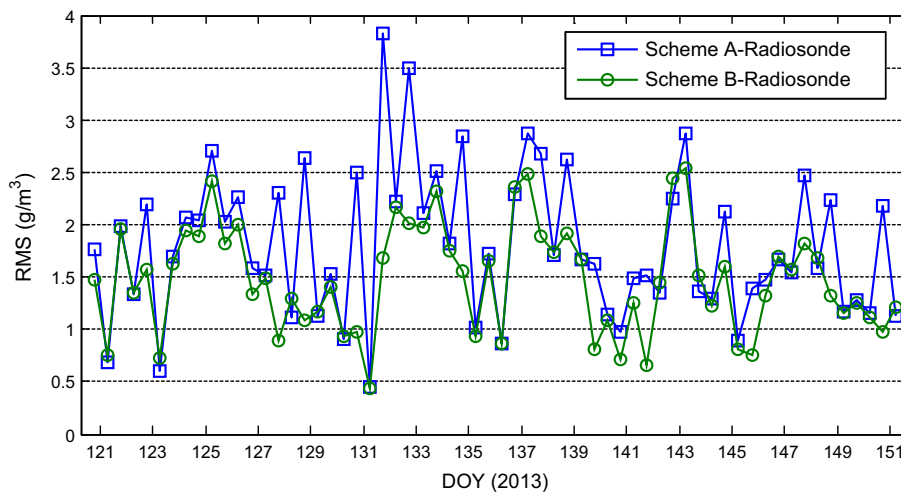


Fig. 14 RMS of scheme A and B compared with radiosonde for 31 days for the period of DOY 121 to 151, 2013



performed at two dates, UTC 00:00 DOY 121, 2013 and 12:00 DOY 136, 2013 as shown in Fig. 13. The two epochs were selected because they correspond to the minimum and maximum IWV value for the period of 31 test days. In addition, we compared the water vapor density value derived from schemes A and B for 31 days with that from radiosonde for the location of radiosonde station at dates, UTC 00:00 and 12:00. Figures 14 and 15 give the RMS of comparison between radiosonde, ECMWF and schemes A and B for the period of DOY 121 to 151, 2013, respectively. Table 6 gives the statistical result of five schemes for 31 days.

It can be seen from Fig. 13 that the 3D water vapor profile derived from scheme B has a good agreement with that from radiosonde. Compared with radiosonde, the

tomographic result derived from scheme B for two selected epochs (RMS are 1.42 and 0.86 g/m^3 , respectively) are superior to that of scheme A (RMS are 2.01 and 1.55 g/m^3 , respectively), yet both schemes show poor results when compared with ECMWF. Figures 14 and 15 also show that the RMS of scheme B is less than that of scheme A. Table 6 tells us that five schemes may all obtain a reliable tomographic result, and when result derived from radiosonde is regarded as a reference, tomographic results derived from various schemes ($\text{RMS} < 2 \text{ g/m}^3$) are better than those from ECMWF ($\text{RMS} = 2.89 \text{ g/m}^3$). In current applications, radiosonde data is the main resource for numerical weather forecast models, therefore, which makes it possible to improve accuracy of numerical weather forecast models with highly-accurate water vapor information using GNSS

Fig. 15 RMS of scheme A and B compared with ECMWF for 31 days for the period of DOY 121 to 151, 2013

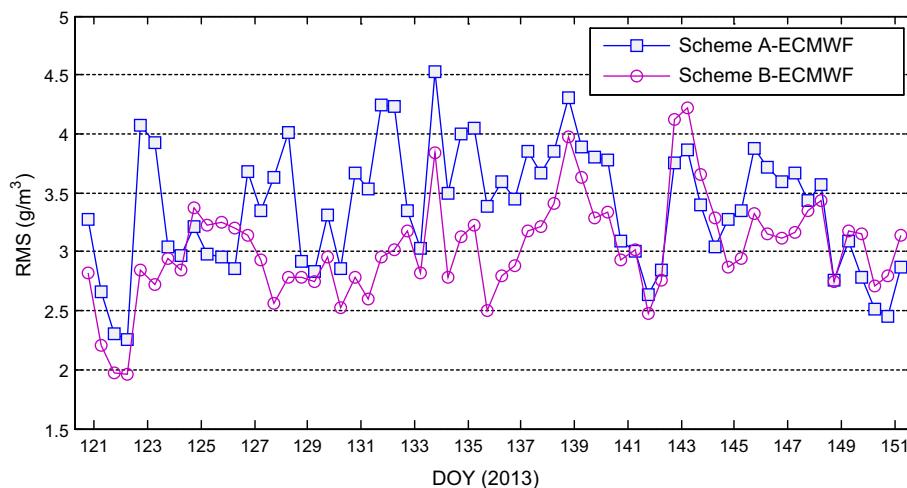


Table 6 Statistical result of water vapor density between radiosonde, ECMWF and different schemes for 31 days for the period of DOY 121 to 151, 2013 (unit: g/m^3)

Data comparison	RMS	STD	MAE	Bias
Radiosonde vs scheme A	1.80	2.01	1.36	-0.06
Radiosonde vs scheme B	1.48	1.57	1.12	-0.02
Radiosonde vs scheme C	1.47	1.57	1.12	-0.02
Radiosonde vs scheme D	1.48	1.58	1.13	-0.02
Radiosonde vs scheme E	1.48	1.58	1.13	-0.02
ECMWF vs scheme A	3.38	2.38	2.99	0.25
ECMWF vs scheme B	3.03	2.37	2.70	0.24
ECMWF vs scheme C	3.02	2.37	2.69	0.24
ECMWF vs scheme D	3.03	2.37	2.70	0.24
ECMWF vs scheme E	3.02	2.37	2.69	0.24
Radiosonde vs ECMWF	2.89	1.62	2.47	0.21

tomographic technique. By comparison we may also conclude that the RMS, STD, MAE and Bias values for tomographic results based on non-uniform symmetrical division of horizontal voxels (scheme B–E) are better than those of traditional method (scheme A).

To further analyze the relationship between vertical water vapor distribution and altitude, the RMS of schemes A and B at different altitudes were calculated in comparison with radiosonde and ECMWF. In addition, we also calculated the relative error using the following formula (Chen and Liu 2014):

$$re = \frac{|\rho - \rho_0|}{\rho} \quad (15)$$

where re is the relative error. ρ_0 is the water vapor density value derived from different tomographic schemes. ρ is the water vapor density value derived from radiosonde or ECMWF.

Figures 16 and 17 give the comparison of RMS and relative error between radiosonde, ECMWF and schemes A and B for the period of DOY 121 to 151, 2013. Relative error and RMS of scheme B are less than those of scheme A, which can be observed from Figs. 16 and 17, further validating the improved nature of the novel method over the traditional method. Generally, relative error increases with altitude because the water vapor density is

Fig. 16 RMS and relative error change with height of various schemes compared with radiosonde for 31 test days

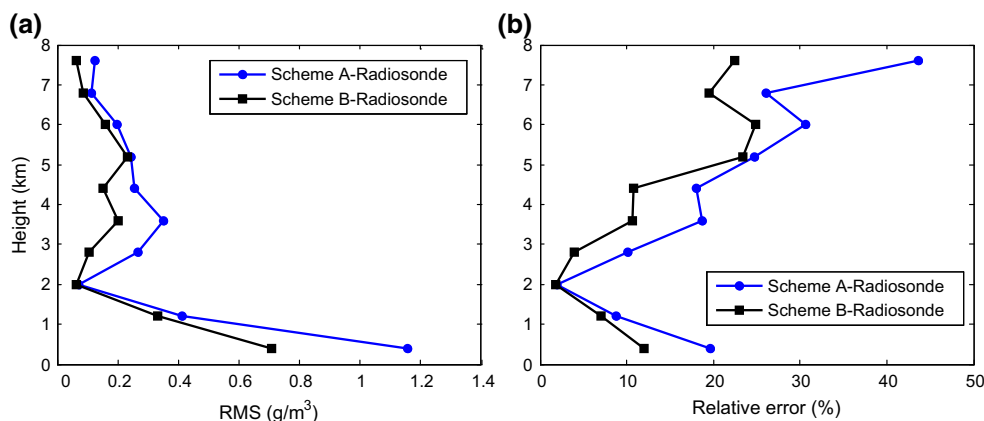


Fig. 17 RMS and relative error change with height of various schemes compared with ECMWF for 31 test days

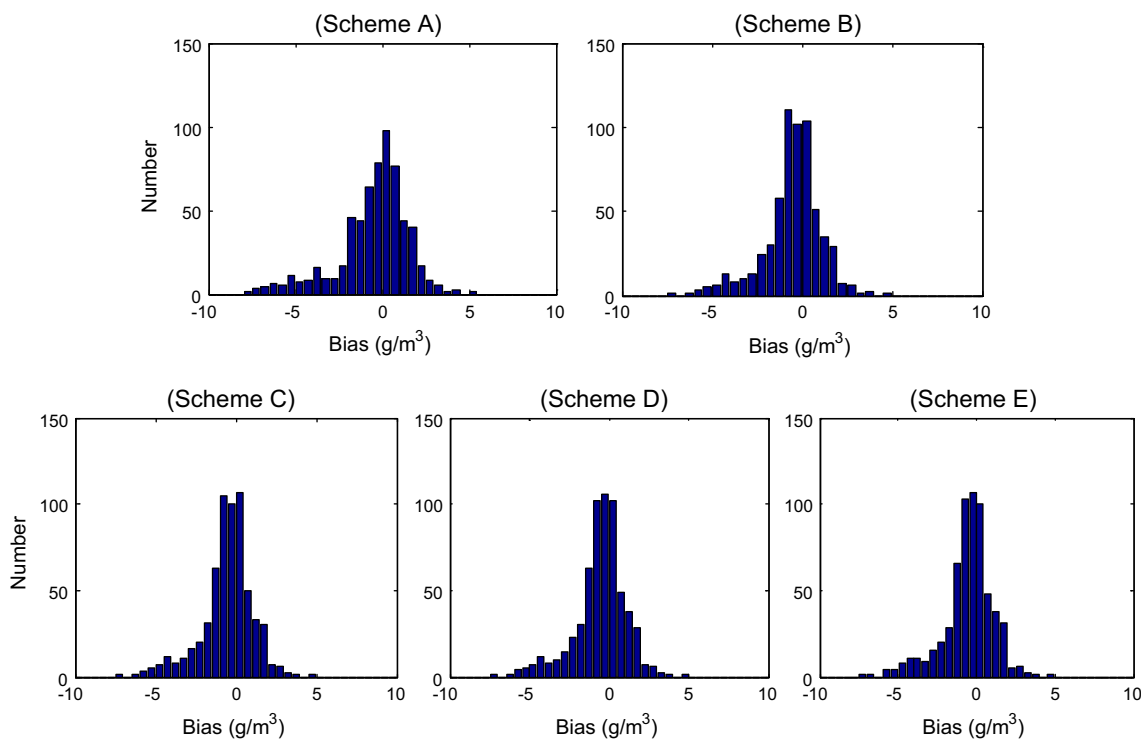
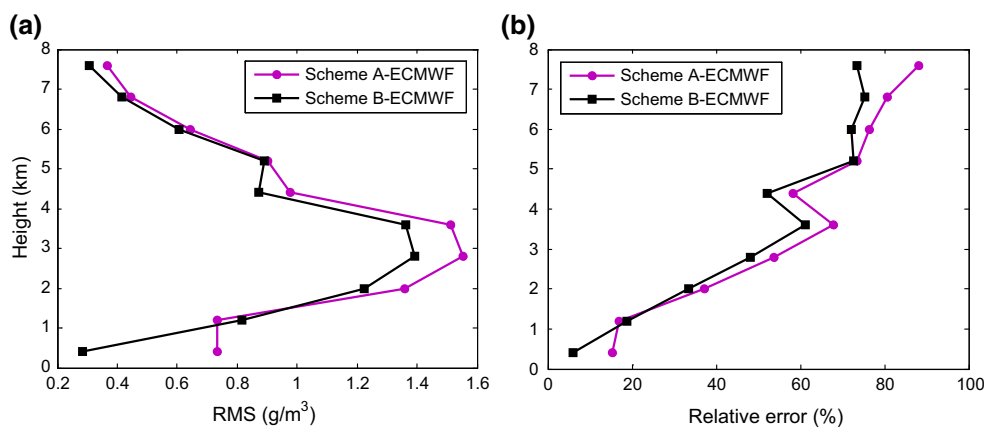


Fig. 18 Error distribution of various schemes for 31 days

very low in the upper layers and a small discrepancy between tomographic result and radiosonde/ECMWF would also lead to a large relative error value.

4.3 Error distribution

The water vapor density derived from radiosonde during the tested period of DOY 121 to 151, 2013 is regarded as the true value, by which we analyzed the error distribution for five schemes. Figure 18 shows the error distribution of various schemes and Table 7 gives the statistical result of error percentage. It can be found from the statistical result

Table 7 Statistical result of error distribution

Scheme	A	B	C	D	E
Percentage (%)	87.42	92.42	92.42	92.26	91.94

that the error distribution is concentrated on -3 to 3 g/m^3 for five tomographic results. From Table 7 we can see that the percentage of schemes B–E are 92.42, 92.42, 92.26 and 91.94 %, separately, which is large than that of scheme A (87.42 %). According to the result mentioned above, we may reasonable to conclude that the error distribution of

Table 8 Statistics of precipitation of rainfall station in King's Park for some days, May 2013 (unit: mm)

DOY	124	126	128	129	130	132	136	137	142	145	150
Precipitation	0	0.5	30.5	14.5	21	3.5	5.5	12	175	48	0

water vapor density derived from tomographic results based on non-uniform symmetrical division of horizontal voxel (scheme B–E) is more closely parallels radiosonde results than that of the traditional method (scheme A).

4.4 The influence of tomographic result under different weather conditions

As shown in Fig. 9, there is a precipitation station which locates at King's park in the tomographic area. The influence of tomographic result was analyzed for some days under different weather conditions according to the rainfall information provided by Hong Kong Observatory. Radiosonde station is next to the rainfall station, the precipitation of rainfall station is thus regarded as a reference, for which Table 8 gives the statistical information for some days in May 2013.

In our study, we analyzed tomographic result of five schemes compared with those derived from radiosonde under different weather conditions for 8 days in May 2013. Table 9 gives the RMS, MAE and Bias values from 8 days for five schemes, while Table 10 gives the statistical result for 8 days. Referring to Tables 9 and 10, one may deduce that all five

Table 9 Comparison of water vapor density between various schemes and radiosonde for 8 days (unit: g/m^3)

Scheme	124	126	128	129	130	136	142	145
RMS								
A	1.88	2.15	1.71	1.88	1.22	1.29	1.43	1.51
B	1.78	1.91	1.10	1.12	1.17	1.26	1.05	1.21
C	1.79	1.90	1.09	1.11	1.17	1.25	0.99	1.25
D	1.81	1.90	1.09	1.13	1.16	1.26	1.02	1.22
E	1.83	1.89	1.09	1.11	1.16	1.25	0.96	1.30
MAE								
A	1.23	1.47	1.26	1.42	0.87	1.05	1.12	1.31
B	1.21	1.31	0.89	0.82	0.80	1.05	0.69	1.01
C	1.22	1.30	0.88	0.80	0.80	1.05	0.64	1.07
D	1.25	1.30	0.87	0.82	0.81	1.05	0.67	1.04
E	1.27	1.29	0.88	0.80	0.81	1.05	0.62	1.12
Bias								
A	-0.60	-0.13	-0.69	0.11	0.03	-0.49	0.25	-0.26
B	-0.55	0.14	-0.66	0.13	0.02	-0.42	0.19	-0.06
C	-0.52	0.13	-0.64	0.12	0.02	-0.43	0.19	-0.11
D	-0.54	0.12	-0.59	0.13	0.02	-0.38	0.16	-0.06
E	-0.53	0.09	-0.55	0.11	0.03	-0.38	0.14	-0.11

Table 10 Statistical result of various schemes for 8 days

Scheme	A	B	C	D	E
RMS	1.63	1.33	1.32	1.32	1.32
MAE	1.22	0.97	0.97	0.98	0.98
Bias	-0.22	-0.15	-0.16	-0.14	-0.15

schemes are able to yield reliable tomographic results under different weather conditions. In addition, the accuracy of tomographic result on the basis of non-uniform symmetrical division of horizontal voxels (scheme B–E) is closer to the true value than that of traditional method (scheme A).

4.5 SWV comparison

To further show the superiority of proposed method, we selected data from different weather conditions for 8 days based on Table 8. Only eleven stations in the research area are used to carry out the tomographic experiment, while the other station (HKSL) is considered as a tested station under the condition that other settings are unchanged. Calculated using observed GPS and meteorological data, and regarded as the true value, the SWV of signal rays from HKSL station pass through the entire test area. Thereby, the comparison between SWV calculated by GPS-observed and meteorological data and SWV derived from tomographic results of various schemes is performed 1 h per day, Shown in Table 11 are the average RMS and MAE calculated from different schemes for 8 days. Table 12 gives the statistical result for 8 days.

Tables 11 and 12 reveal that RMS and MAE value of schemes B–E are less than those of scheme A, while the differences between scheme B to scheme E are very slight. This shows that the accuracy of the proposed method (scheme B–E) is higher than that of traditional method (scheme A), and further exhibit the superiority of proposed method.

5 Conclusion

A novel, optimized approach of voxel division has been proposed for water vapor tomography. In this study, the vertical boundary is determined based on the 3D water vapor profile derived from radiosonde for 40 years, which avoids the waste of observation data in selecting vertical

Table 11 RMS of SWV for different schemes for 8 days (Unit: mm)

Scheme DOY	RMS					MAE				
	A	B	C	D	E	A	B	C	D	E
124	5.99	4.96	4.98	4.88	4.91	4.00	2.94	3.02	2.92	2.91
126	7.11	6.63	6.49	6.51	6.43	5.36	4.32	4.27	4.29	4.29
128	9.80	8.19	8.17	8.13	8.16	7.27	5.36	5.34	5.40	5.38
132	12.72	11.56	11.88	11.60	12.02	7.94	6.48	6.72	6.53	6.83
137	8.44	7.91	7.98	7.91	8.07	7.05	6.33	6.45	6.31	6.49
142	19.87	18.27	18.57	18.49	18.95	12.43	10.35	10.57	10.41	10.73
145	14.77	12.52	13.08	12.45	13.04	7.52	6.07	6.23	6.02	6.22
150	11.18	10.09	10.30	10.38	10.49	8.15	7.38	7.57	7.39	7.52

Table 12 Statistical result of various schemes for 8 days

Scheme	A	B	C	D	E
RMS	11.24	10.16	10.18	10.04	10.26
MAE	7.47	6.15	6.27	6.16	6.30

boundary based on experiences. In horizontal direction, the concept of non-uniform symmetrical division of horizontal voxels is proposed on the basis of actual distribution of signals passing through the tomographic area.

Five schemes are designed based on above idea to validate the proposed method, on which experiments were performed using data from the GPS network across all of May 2013. Radiosonde and ECMWF data are both used here to test the tomographic result. The result shows that between radiosonde, ECMWF and the five schemes, the RMS, STD, MAE and Bias values of tomographic result derived from the proposed approach are superior to that of traditional method. Therefore, if the principle of horizontal voxel division is followed according to the proposed method, a preferable result would be obtained than that of traditional method. The selecting method of top boundary and voxel division proposed in the paper provides a reference for water vapour tomography study, which enhances the utilization of signals used and the number of voxels crossed by rays, and has very important application value as well.

Acknowledgments The authors would like to thank IGAR for providing access to the web-based IGAR data and ECMWF for providing grids data of temperature, relative humidity and so on. The Lands Department of HKSAR is also acknowledged for providing GPS data from the Hong Kong Satellite Positioning Reference Station Network (SatRef) and rainfall information. This research was supported by the National Natural Science Foundation of China (41174012).

References

Adavi Z, Mashhadi-Hossainali M (2014) 4D tomographic reconstruction of the tropospheric wet refractivity using the concept of

- virtual reference station, case study: northwest of Iran. *Meteorol Atmos Phys* 126(3–4):193–205
- Adeyemi B, Joerg S (2012) Analysis of water vapor over Nigeria using radiosonde and satellite data. *J Appl Meteorol Climatol* 51:1855–1866. doi:10.1175/JAMC-D-11-0119.1
- Alber C, Ware R, Rocken C, Braun J (2000) Obtaining single path phase delays from GPS double differences. *Geophys Res Lett* 27(17):2661–2664
- Bender M, Dick G, Ge M et al (2011) Development of a GNSS water vapour tomography system using algebraic reconstruction techniques. *Adv Space Res* 47:1704–1720. doi:10.1016/j.asr.2010.05.034
- Bevis M, Businger S, Herring TA et al (1992) GPS meteorology: remote sensing of atmospheric water vapor using the global positioning system. *J Geophys Res* 97:15787–15801
- Bi YM, Mao J, Li C (2006) Preliminary results of 4d water vapor tomography in the troposphere using GPS. *Adv Atmos Sci* 23:551–560. doi:10.1007/s00376-006-0551-y
- Brenot HV, Ducrocq A, Walpersdorf C et al (2006) GPS zenith delay sensitivity evaluated from high-resolution numerical weather prediction simulations of the 8–9 September 2002 flash flood over southeastern France. *J Geophys Res* 111:D15105. doi:10.1029/2004JD005726
- Champollion C, Flamant C, Bock O et al (2009) Mesoscale GPS tomography applied to the 12 June 2002 convective initiation event of IHOP 2002. *Q J R Meteorol Soc* 135:645–662
- Champollion C, Masson F, Bouin MN et al (2005) GPS water vapour tomography: preliminary results from the ESCOMPTE field experiment. *Atmos res* 74(1):253–274
- Chen BY, Liu ZZ (2014) Voxel-optimized regional water vapor tomography and comparison with radiosonde and numerical weather model. *J Geod* 88:391–703. doi:10.1007/s00190-014-0715-y
- Elósegui P, Ruis A, Davis JL, Ruffini G, Keilm SJ, Bürki B, Kruse LP (1998) An experiment for estimation of the spatial and temporal variations of water vapor using GPS data. *Phys Chem Earth* 23:125–130
- Flores A, Ruffini G, Rius A (2000) 4D tropospheric tomography using GPS slant wet delays. *Ann Geophys* 18:223–234. doi:10.1007/s00585-000-0223-7
- Herring TA, King RW, McClusky SC (2010) Documentation of the GAMIT GPS Analysis Software release 10.4. Department of Earth and Planetary Sciences, Massachusetts Institute of Technology, Cambridge, Massachusetts
- Liu YX, Chen YQ, Liu JN (2001) Determination of weighted mean tropospheric temperature using ground meteorological measurements. *Geospatial Inf Sci* 4(1):14–18
- Liu ZZ, Wong MS, Nichol J, Chan PW (2013) A multi-sensor study of water vapour from radiosonde, MODIS and AERONET: a

- case study of Hong Kong. *Int J Climatol* 33:109–120. doi:[10.1002/joc.3412](https://doi.org/10.1002/joc.3412)
- Mendes VB (1999) Modeling the neutral-atmosphere propagation delay in radiometric space technique. PhD dissertation, University of New Brunswick, Fredericton, New Brunswick, Canada
- Mohanakumar K (2008) Structure and composition of the lower and middle atmosphere. *Stratosphere Troposphere Interactions: An Introduction*, Springer, Netherlands p 1–53
- Niell AE, Coster AJ, Solheim FS et al (2001) Comparison of measurements of atmospheric wet delay by radiosonde, water vapor radiometer, GPS, and VLBI. *J Atmos Ocean Technol* 18:830–850
- Notarpietro R, Cucca M, Gabella M et al (2011) Tomographic reconstruction of wet and total refractivity fields from GNSS receiver networks. *Adv Space Res* 47:898–912. doi:[10.1016/j.asr.1012.12.025](https://doi.org/10.1016/j.asr.1012.12.025)
- Perler D, Geiger A, Hurter F (2011) 4D GPS water vapour tomography: New parameterized approaches. *J Geophys Res* 85:539–550
- Ran BY, Ge WZ (1997) Singular value decomposition method compared with damping least square method. *Geophys Comput Technol* 1:46–49
- Rocken C, Hove TV, Johnson J, Solheim F, Ware R, Bevis M, Businger S (1995) GPS/STORM-GPS sensing of atmospheric water vapor for meteorology. *J Atmos Ocean Technol* 12(3):468–478
- Rohm W, Bony J (2009) Local tomography troposphere model over mountains area. *Atmos Res* 93:777–783. doi:[10.1016/j.atmosres.2009.03.013](https://doi.org/10.1016/j.atmosres.2009.03.013)
- Rohm W, Zhang K, Bony J (2014) Limited constraint, robust Kalman filtering for GNSS troposphere tomography. *Atmos Meas Tech* 7(5):1475–1486
- Saastamoinen J (1972) Atmospheric correction for the troposphere and stratosphere in radio ranging satellites. *The use of artificial satellites for geodesy*, p 247–251
- Skone S, Hoyle V (2005) Troposphere modeling in a regional GPS network. *J Glob Position Syst* 4:230–239
- Song S, Zhu W, Ding J, Peng J (2006) 3D water vapor tomography with Shanghai GPS network to improve forecasted moisture field. *Chin Sci Bull* 51:607–614
- Troller M, Bürki B, Cocard M, Geiger A, Kahle H-G (2002) 3-D refractivity field from GPS double difference tomography. *Geophys Res Lett* 29:2149–2152
- Wan R (2014) Research progress of the unconventional observing technology and the data used in the study of rainstorm in China. *Adv Meteorol Sci Technol* 4:24–35
- Wang JK, Han SQ, Bian H et al (2014) Characteristics of the three-dimensional GPS tomography water vapor field during the rainstorm. *Acta Sci Nat Univ Pekin* 50:1053–1064
- Yao YB, Zhao QZ, Zhang B (2016) A method to improve the utilization of GNSS observation for water vapor tomography. *Ann Geophys* 34:143–152